ROYAL SOCIETY
OF CHEMISTRY

PAPER

Check for updates

Phase transformations in the nickel phosphide system induced by transition-metal doping and their electro-catalytic study†

Gwaza E. Ayom, [ID] [a] Malik D. Khan, [ID] [ab] Siphamandla C. Masikane, [ID] [a] Felipe M. de Souza,[c] Wang Lin,[c] Ram K. Gupta[c] and Neerish Revaprasadu [ID] *[a]

Nickel phosphide exists in various compositions, and the synthesis of pure-phase nickel phosphides is of immense interest due to their wide scale applications in different electrocatalytic reactions. We report the facile synthesis of nickel phosphides and rare transition metal-induced phase transformations within this system. Phase selective synthesis of pure Ni_2P or Ni_5P_4 was achieved by decomposition of nickel acetate tetrahydrate $Ni(AC)_2 \cdot 4H_2O$ in optimized mixed solvent systems, *i.e.*, in tri-octylphosphine oxide (TOPO)/tri-*n*-octylphosphine (TOP) or hexadecylamine (HDA)/TOP, respectively, by hot injection route. The doping of 5% Cu or Mn in either of the nickel phosphide phases yielded a mixture of phases (Ni_2P/Ni_5P_4). However, increasing the Cu or Mn content to 10% resulted in the complete transformation of phase, *i.e.*, from Ni_2P to pure Ni_5P_4 and *vice versa*. Lattice stress and size of incorporated dopants, as well as the nature of surfactants employed, were discussed as probable causes of these rare phase transformations. Moreover, in order to establish structure–activity relationship, we studied the comparative effect of transition metal dopants in both nickel rich and nickel deficient phases. Therefore, initially formed and transformed phosphides were investigated as electrocatalysts for overall water splitting and supercapacitance. NiP-5 (Ni_2P formed on 10% Cu doping of Ni_5P_4) delivered a current density of 10 mA cm^{-2} with the lowest overpotential of 146 mV among all samples for HER while NiP-3 (Ni_5P_4 formed from Ni_2P on 10% Cu doping) similarly required the least overpotential of 276 mV for the OER at the same current density. NiP-2 (pristine Ni_5P_4) had the highest calculated specific capacitance of 1325 F g^{-1} at 2 A g^{-1}. These phase transformations resulted in better catalytic activity and stability as well as reaction kinetics indicating suitability in practical water splitting technologies.

Introduction

Transition metal phosphides, in particular nickel phosphides, are of interest to materials scientists due to their applications in energy storage,[1–3] energy generation,[4] bio-sensing[5] and catalytic recycling.[6] Reports on nickel phosphides are limited compared to the sulfide analogs because their preparation is constrained by factors such as toxicity, prolonged reaction times, elevated temperatures and multiple starting precursors.[3]

The reactions that evolve hydrogen and oxygen (water splitting) at the electrodes continue to attract attention from the scientific community. This is due to the potential of these reactions changing our planet's over-reliance on fossil fuels for its energy requirements.[7] Water splitting reactions, unlike fossil fuels, lead to the formation of non-carbon based and recyclable fuels. However, these reactions are constrained by expensive and scarce noble metal catalysts such as Pt and Ir.[8] Cheaper and readily available alternatives like nickel phosphides have been investigated in place of noble metals.[2,9] Nickel phosphides have been reported to be excellent catalysts not only in energy conversion reactions like water splitting[2,9,10] but also suitable for energy storage applications such as supercapacitance.[11,12]

Synthetic protocols to nickel phosphides include phosphatization of nickel with phosphines,[13] topochemical transformations of phosphorene nanosheets to nickel phosphide by nickel salts,[14] solvothermal decompositions,[2,15] microwave combustion[16] and solvent-less synthesis.[17] The use of single-source precursors to prepare nickel phosphides has generated much interest compared to dual or multiple precursors owing to the ease and simplicity of this synthetic route. However, the synthesis of nickel phosphide using single-source precursors is hindered by factors like ligand design and metal complexation

[a]Department of Chemistry, University of Zululand, Private Bag X1001, KwaDlangezwa 3880, South Africa. E-mail: RevaprasaduN@unizulu.ac.za

[b]Institute of Physical Chemistry, Polish Academy of Sciences, Kasprzaka 44/52, 01-224, Warsaw, Poland

[c]Department of Chemistry, Kansas Polymer Research Center, Pittsburg State University, Pittsburg, KS 66762, USA

† Electronic supplementary information (ESI) available: Powder-XRD patterns, SEM images and SEM-EDX elemental mapping images of formed materials and comparison tables for HER, OER and supercapacitance. See DOI: 10.1039/d1se01866c

to meet desired materials. Moreover, nickel phosphide exists in multiple compositions ranging from the phosphorus-rich phases such as NiP_3, NiP_2 and Ni_5P_4 to phosphorus-deficient phases like Ni_3P, Ni_2P and NiP.[18] The multiplicity of phases and compositions is a great strain on the preparation of pure or desired nickel phosphide phases.

The doping of nickel phosphide with foreign atoms is a common strategy used to tune and improve the physical and electronic properties of these systems. For example, Guo *et al.* recently fabricated an Fe-doped Ni_2P electrocatalyst for electro-reduction of nitrogen to ammonia.[19] Other researchers have also introduced foreign atoms like Fe, Ru, Mn and N into the crystal lattice of nickel phosphide to improve its performance as a catalyst in hydrogen/oxygen evolution reactions and super-capacitance.[20–23] Doping may also result in alterations and inter-ruptions of the regular atomic arrangements in nickel phosphide, which could lead to materials that have greater functionality.[24]

Structural phase transformation of metal oxide/chalcogenides influenced by doping has been previously re-ported. For example, Hasti *et al.* reported transformations from monoclinic to tetragonal VO_2 nanowires induced by W doping.[25] Zheng *et al.* demonstrated structural transitions from cubic to orthorhombic $CoSe_2$ prompted by phosphorus doping.[26] Researchers have also reported structural phase trans-formations in Mo and W chalcogenides mediated by chemical and mechanical exfoliation of the layered compounds.[27–30] The thermal route as a mediator of phase transformations in Se, Te and Ni chalcogenides has also been studied.[31,32] There are, however, limited reports on this kind of phase transformation within the metal phosphide system. For example, secondary phase transformations of preformed $Ni_{12}P_5$ nanoparticles to Ni_2P, by employing TOP as the phosphorus source, have been reported.[33] Furthermore, urea and polyethylene glycol have been explored as additives to mediate hexagonal Ni_2P to tetragonal $Ni_{12}P_5$ transformations though these reactions employed the hazardous red phosphorus and extended reaction times.[34,35] Phase transformations in the nickel phosphide system could be very advantageous considering the difficulty in preparation of pure/desired phases in this multi-phased system and their diverse functionalities.

Herein, we report (i) the facile preparation of Ni_2P and Ni_5P_4 nanoparticles using nickel acetate tetrahydrate ($Ni(AC)_2 \cdot 4H_2O$) as the nickel source, tri-*n*-octyl phosphine (TOP) as the phosphorus source, and tri-octyl-phosphine oxide (TOPO) or hexadecylamine (HDA) as the surfactants in a hot injection method, (ii) primary phase transformations (Ni_2P to Ni_5P_4 when employing TOPO/TOP or Ni_5P_4 to Ni_2P when employing HDA/TOP) in the nickel phos-phide system on doping Ni_2P or Ni_5P_4 with $Cu(AC)_2 \cdot H_2O$ and $Mn(AC)_2$, respectively and (iii) the effect of doping/phase trans-formations on the overall water splitting and supercapacitance performance of the prepared nickel phosphide catalysts.

Experimental details

Materials

Hexadecylamine (HDA) 98%, tri-*n*-octylphosphine (TOP) 90%, tri-octylphosphine oxide (TOPO) 90%, nickel acetate

tetrahydrate ($Ni(CH_3COO)_2 \cdot 4H_2O$), copper acetate mono-hydrate ($Cu(CH_3COO)_2 \cdot H_2O$), manganese acetate ($Mn(CH_3COO)_2$), chloroform, methanol and acetone were purchased from Sigma-Aldrich and used without further purification.

Preparation of nanoparticles

(a) Ni_2P. Ni_2P nanoparticles were prepared by the colloidal thermolysis of nickel acetate tetrahydrate ($Ni(AC)_2 \cdot 4H_2O$) in the presence of the dispersing solvent TOP and the surfactant TOPO. In a typical procedure, TOPO (5.0 g) was heated under N_2, up to 300 °C, and injected quickly with $Ni(AC)_2 \cdot 4H_2O$ (0.50 g, 2.01 mmol) dispersed in TOP (5.0 mL), yielding an immediate black solution. The reaction temperature dropped to about 280 °C upon injection, and the reaction mixture was heated up again to 300 °C. The temperature was maintained at 300 °C for 1 h, after which the reaction mixture was cooled down naturally to about 70 °C. Methanol/acetone (20 mL, 1 : 1) mixture was then added to the cooled black solution, and the precipitate was washed and isolated by centrifugation.

(b) Ni_5P_4. The preparation of Ni_5P_4 nanoparticles followed a similar procedure as (a) above, except that HDA replaced TOPO as the surfactant. The formation of Ni_5P_4 also involved an extra washing step with a mixture of chloroform and methanol (10 mL, 1 : 4 ratio), and then finally acetone (10 mL).

(c) Preparation of 5 and 10% Cu or Mn-doped Ni_2P. $Cu(AC)_2 \cdot H_2O$ (0.020 g, 0.101 mmol) for 5% Cu or $Cu(AC)_2 \cdot H_2O$ (0.040 g, 0.201 mmol) for 10% Cu doping was mixed with $Ni(AC)_2 \cdot 4H_2O$ (0.50 g, 2.01 mmol) and dispersed in TOP (5 mL) by sonication. The dispersed mixture was quickly injected into a hot solution of TOPO at 300 °C yielding an immediate black solution. The black solution was heated at 300 °C for one hour, cooled to 70 °C, and precipitated with methanol/acetone solution. Black precipitates of doped nanoparticles were washed with acetone, isolated by centrifugation, and air-dried. For 5% Mn and 10% Mn doping, $[Mn(AC)_2$ (0.017 g 0.101 mmol)] or $[Mn(AC)_2$ (0.035 g, 0.201 mmol)] was used in place of $Cu(AC)_2 \cdot H_2O$, respectively.

(d) Preparation of 5 and 10% Cu or Mn-doped Ni_5P_4. The preparation of 5 and 10% Cu or Mn doping of Ni_5P_4 nano-particles followed a similar procedure as (c) above, except that HDA replaced TOPO as the surfactant. These preparations also followed the extra washing step outlined in (b) above.

(e) Preparation of Ni_2P, Cu or MnO in TOP. To TOP (5 mL) at 300 °C, $Ni(AC)_2 \cdot 4H_2O$ (0.50 g, 2.01 mmol) or $Cu(AC)_2 \cdot 4H_2O$ (0.040 g, 0.201 mmol) or $Mn(AC)_2$ (0.035 g, 0.201 mmol) dispersed in TOP (5 mL) was injected, yielding a black or brown or milky precipitate, respectively. The temperature was main-tained at 300 °C for 1 h, after which the precipitates were iso-lated as stated in the procedure (a) above. The same procedure was employed for the Cu and Mn-doped Ni_2P (in the decom-position of $Ni(AC)_2 \cdot 4H_2O$ in TOP) except for the addition of 10% moles of $Cu(AC)_2 \cdot H_2O$ or 10% moles of $Mn(AC)_2$ to $Ni(CH_3COO)_2 \cdot 4H_2O$ before decomposition as stated in (c) above.

Instrumentation

X-ray diffraction was performed using a Bruker D8 Discover Diffractometer using Cu $K\alpha$ radiation ($\lambda = 1.54178$ Å) in the 2θ

range from 10° to 70°. The data collected were used to determine the lattice parameters and crystal phase. Scanning electron microscopy (SEM) was carried out using Philips XL30 FEG-SEM. Energy-dispersive X-ray (EDX) spectroscopy was performed using a DX4 detector. All samples were carbon-coated using an Edwards coating system E306A before SEM analysis. Transmission electron microscopy (TEM) images of the materials were acquired employing a JEOL TEM (1400) instrument.

Electrochemical studies

Electrochemical characterization of the prepared nickel phosphides was performed using a Versastat 4-500 electrochemical workstation (Princeton Applied Research, USA), which employed a three-electrode system. Electrode preparation of the nickel phosphides for electrochemical investigations was done by forming pastes of these particles (80 wt%), polyvinylidene difluoride (PVDF, 10 wt%), and acetylene black (10 wt%). Acetylene black was prepared using the solvent N-methyl pyrrolidinone (NMP). These formed pastes were then applied to nickel foams (MTI Corporation, USA, 99.99% purity) that were precleaned and pre-weighted. Commercial carbons (MTI Corporation, USA) were used as conducting acetylene black with particle sizes ranging between 35 and 40 nm. Platinum wires were utilized as counter electrodes, while saturated calomel electrodes (SCE) were used as reference electrodes. Supercapacitance and electro-catalytic investigations were carried out using 3 M and 1 M KOH electrolyte, respectively. Charge storage capacity was measured using cyclic voltammetry (CV), electrochemical impedance spectroscopy (EIS), and galvanostatic charge–discharge (CD) at various scan rates and current densities. Electro-catalytic properties of the prepared nickel phosphide electrodes were investigated via CV and linear sweep voltammetry (LSV), with LSV done at a scan rate of 2 mV s^{-1} for HER/OER measurements. EIS was performed in the frequency range of 0.05 Hz to 10 kHz with an AC amplitude of 10 mV.

Results and discussion

Nickel phosphide nanoparticles were synthesized by the hot injection method with nickel acetate tetrahydrate (Ni(Ac)$_2$·4H$_2$O) as the nickel source, tri-n-octylphosphine (TOP) as the phosphorus source, and tri-octyl-phosphine oxide (TOPO) or hexadecylamine (HDA) as the surfactants. The decomposition of Ni(Ac)$_2$·4H$_2$O in TOPO/TOP for an hour formed nickel phosphide, which was indexed to phase-pure hexagonal Ni$_2$P (ICDD #03-065-1989), herein referred to as NiP-1 as shown in the powder-XRD patterns (Fig. 1a).

The decomposition of the same precursor (Ni(Ac)$_2$·4H$_2$O) under similar reaction conditions but with HDA in place of TOPO yielded a different phase of nickel phosphide (Fig. 1b), which was indexed to phase-pure hexagonal Ni$_5$P$_4$ (ICDD #01-089-2588) and is henceforth referred to as NiP-2. The formation of NiP-1 or NiP-2 from the decomposition of the same precursor in similar conditions employing TOPO/TOP or HDA/TOP does suggest that the surfactants play a key role in the phase of the formed nickel phosphide. These results are comparable with
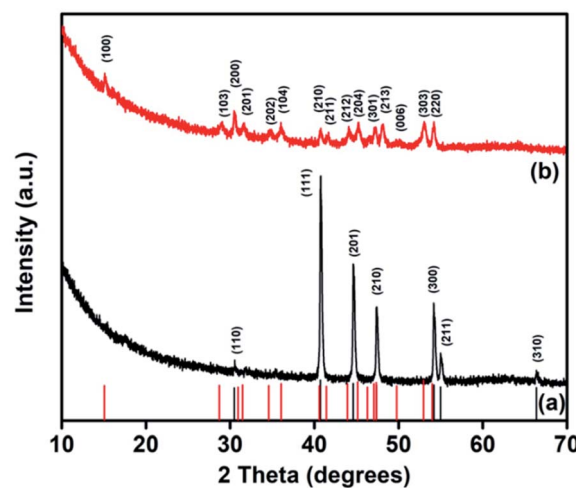

Fig. 1 Powder-XRD patterns of the decomposition of Ni(Ac)·4H$_2$O in (a) TOPO/TOP and (b) HDA/TOP at 300 °C for 1 h.

our earlier study where a dithiophosphonate complex of nickel was employed as a single source precursor to prepare either NiP-1 or NiP-2 particles using TOPO/TOP or HDA/TOP.[2] Chemists have played with different surfactants as a tool to influence the phase of formed nickel phosphides while employing Ni(Ac)$_2$·4H$_2$O as the nickel source. For example, the Tatsumisago group[36] has reported the formation of NiP$_2$ by refluxing a mixture of Ni(Ac)$_2$·4H$_2$O, TOPO and TOP at 360 °C for 5 hours. Similarly, Ni$_2$P was formed when heating a mixture of the same nickel precursor (Ni(Ac)$_2$·4H$_2$O), TOP, n-octyl ether, and oleylamine at 350 °C for 1 hour.[12] The surface adsorption[37] and passivation[38] effect of surfactants on the prepared nanomaterials have been studied. HDA with a linear structure binds to the surface of the nanoparticles via the lone pair of electrons on the nitrogen atom while the branched TOPO caps the nanoparticles through the lone pair of electrons on the oxygen atom. Moreover, the passivation of the prepared particles by linearly shaped surfactants such as HDA can leave pockets of space during capping, which can lead to surface oxidation,[39] unlike branched surfactants (TOPO) that protect the surface of nanoparticles better comparatively, leading to enhanced stability. The surface adsorption and passivation effects of surfactants used in this study (TOPO/HDA) could be one of the factors that explain the formation of different phases of nickel phosphides using the same nickel precursor.

Both phases of nickel phosphides (NiP-1 and NiP-2) were doped with Cu or Mn employing Cu(Ac)$_2$·H$_2$O or Mn(Ac)$_2$ as the metal source, respectively. A careful examination of Cu-doping in Ni$_2$P in TOPO/TOP indicates a gradual phase transformation from Ni$_2$P (NiP-1) to Ni$_5$P$_4$ (NiP-3), as depicted in Fig. 2(I). For instance, the p-XRD peaks of 5% Cu doped NiP-1 indicate the formation of a mixture of phases. The major phase is indexed to Ni$_5$P$_4$ and diffraction peaks of the NiP-1 phase at (201), (210) and (211) [asterisked peaks of Fig. 2(I)b] were also present as a minor phase.

The intensity of the peaks for NiP-1 starts to decrease in 5% Cu doped NiP-1 [Fig. 2(I)b] and disappeared in 10% Cu doping
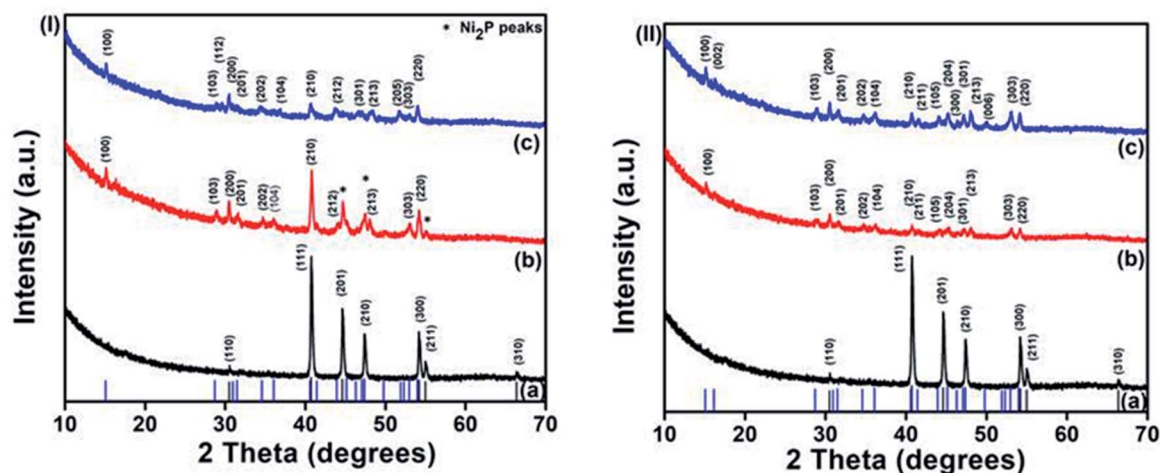

Table 1 Summary of formed nickel phosphides and their phase transformations from the decompositions of $Ni(Ac)_2 \cdot 4H_2O$ in different solvents for one hour

Nickel precursor	Solvents	Dopants	Formed phase
$Ni(Ac)_2 \cdot 4H_2O$	TOPO/TOP	—	NiP-1 (Ni_2P)
$Ni(Ac)_2 \cdot 4H_2O$	TOPO/TOP	5% Cu	$Ni_5P_4 + Ni_2P$
$Ni(Ac)_2 \cdot 4H_2O$	TOPO/TOP	10% Cu	NiP-3 (Ni_5P_4)
$Ni(Ac)_2 \cdot 4H_2O$	TOPO/TOP	5% Mn	Ni_5P_4
$Ni(Ac)_2 \cdot 4H_2O$	TOPO/TOP	10% Mn	NiP-4 (Ni_5P_4)
$Ni(Ac)_2 \cdot 4H_2O$	HDA/TOP	—	NiP-2 (Ni_5P_4)
$Ni(Ac)_2 \cdot 4H_2O$	HDA/TOP	5% Cu	$Ni_2P + Ni_5P_4$
$Ni(Ac)_2 \cdot 4H_2O$	HDA/TOP	10% Cu	NiP-5 (Ni_2P)
$Ni(Ac)_2 \cdot 4H_2O$	HDA/TOP	5% Mn	Ni_2P
$Ni(Ac)_2 \cdot 4H_2O$	HDA/TOP	10% Mn	NiP-6 (Ni_2P)

2 to NiP-5 is observed at 10% Cu doping [Fig. 3(II)c], since there are no residual peaks of NiP-2. Scheme 1 gives a perspective flow of the formed nickel phosphides in this study and the transformations in the nickel phosphide system induced by transition metal-doping.

Similarly, we obtained pure Ni_2P (NiP-6) on doping NiP-2 (Ni_5P_4) formed from the decomposition of $Ni(Ac)_2 \cdot 4H_2O$ in HDA/TOP with Mn as shown in Fig. 3(II) [ICDD #03-065-1989]. The higher intensity of the XRD peaks of the 10% Mn doping compared to that of 5% doping (Fig. 3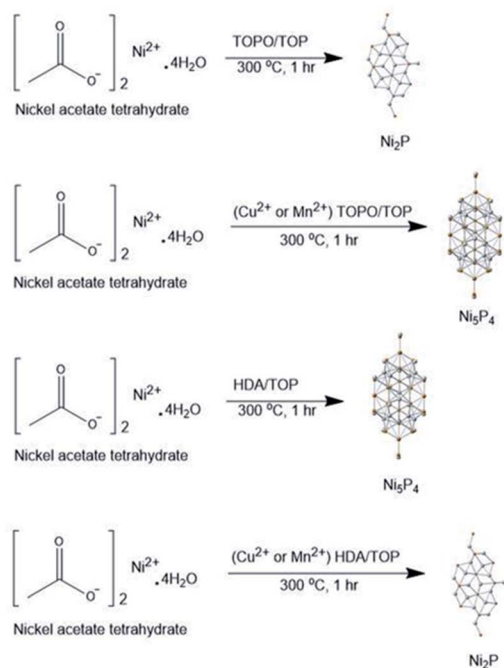(II)b and c) could be indicative of a complete phase transformation from NiP-2 to NiP-6 similar to the reverse transformations stated earlier (Fig. 2). These findings show that the phase transformations from NiP-2 to NiP-6 on doping the NiP-2 formed on the decomposition of $Ni(Ac)_2 \cdot 4H_2O$ in HDA/TOP with Cu is gradual,

whereas the Mn doping shows a faster transformation comparatively. Table 1 summarizes the nickel phosphides formed from the decomposition of $Ni(Ac)_2 \cdot 4H_2O$ in different solvents and the phase transformations in the nickel phosphide system upon doping with different amounts of Cu and Mn.

The structural transformation from one phase to another for transition metal chalcogenides mediated by chemical or thermal means has been reported in the literature,[26,36,40,41] though to the best of our knowledge, a phase transformation from one pure phase nickel phosphide to another induced by doping a foreign atom into its crystal lattice has not been reported. In a previous study, Xu *et al.* also indicated the formation of a mixture of Ni_2P and Ni_5P_4 phases upon Mn-doping *via* a hydrothermal route, whereas Sarkar *et al.* observed that the incorporation of Mn induces tensile stress in Ni_2P lattice structure.[22,42] Saurav *et al.* similarly demonstrated that the doping of Cu into $Pd_{17}Se_{15}$ *via* a colloidal route induces tensile stress in the palladium selenide's crystal lattice that subsequently modifies its lattice parameters.[43] The incorporation of Mn or Cu into the formed phosphides, therefore may have induced tensile stress in these materials that resulted in the phase transformations observed. The reasons behind the formation of a particular phase and its transformation are not clear or well understood though there have been reports of phase transformations induced by nature of nickel precursor used, phosphorus to nickel ratio, reaction temperature and time or vacant defects generated by the dopants.[26,36,40,44] Phosphidating agents such as TOP could therefore play a key role in the diffusion of phosphorus in or out of metals depending on the chemical environment during metal phosphide formation. In the quest to find out the type of stress or defects created by the incorporation of dopants, the decomposition of copper and manganese acetate salts were also explored separately, under similar reaction conditions. The p-XRD analysis of the product obtained after the decomposition of $Cu(AC)_2 \cdot H_2O$ in TOPO/TOP or HDA/TOP showed the formation of face-centered cubic Cu metal (Fig. S1†). Likewise, $Mn(AC)_2$ also didn't form manganese phosphide on decomposition in TOPO/TOP or HDA/TOP, rather the formation of manganese oxide was observed (Fig. S2†). It is pertinent to note that the decomposition of $Cu(AC)_2 \cdot H_2O$ or $Mn(AC)_2$ in TOP alone in the same laboratory conditions also formed Cu or MnO, respectively, as shown in Fig. S1 and S2.† The mixing of two compounds is more feasible when they have similar oxidation states and exist in a similar crystal structure. For example, both Cu_3P and Ni_2P are hexagonal; therefore Cu_3P would have fit easily into the hexagonal lattice structure of Ni_2P, causing minimal lattice stress.[45] As the dopant metals (Cu and Mn) do not form their respective metal phosphides separately under similar reaction conditions, it is possible that the different products form at the initial stages of the reaction, which may be responsible for creating stress and facilitating the phase transformation. Moreover, the sizes of the dopant ions (Cu^{2+} or Mn^{2+}) employed in this study may also have an effect on the lattice structure. The size of the Mn^{2+} (83 pm) dopant, which is larger than Cu^{2+} (73 pm) as compared to the host Ni^{2+} (69 pm), plausibly promotes the phase transformation. This may

Scheme 1 A schematic perspective to formed phosphides and dopant induced phase transformations in this study.

also explain the faster phase transformation in the nickel phosphide system when doping with Mn compared to Cu.

Likewise, the nature of the surfactants employed may also influence the kinetics of the reaction and facilitate the formation of a particular phase. For instance, TOPO or HDA seem to play a key role in promoting or hindering the diffusion of phosphorus into nickel atoms. Hexadecylamine is a much stronger base than TOPO, and may assist in the decomposition of TOP to release phosphorus which is responsible for phosphide formation. Furthermore, the linear structure of HDA, surrounding nickel atoms, is less effective in hindering the diffusion of phosphorus as compared to the bulky and branched TOPO molecule. Therefore, the phosphorus-rich phase (Ni_5P_4) is favored by HDA, whereas the phosphorus-deficient phase (Ni_2P) was obtained in the presence of TOPO. To investigate the role of the surfactants in these phase transformations, we performed these decomposition reactions in TOP alone, following similar experimental conditions. The decomposition of $Ni(Ac)_2 \cdot 4H_2O$ in TOP at 300 °C for 1 h formed NiP-1 (ICDD #03-065-1989) as seen in Fig. S3a.† In addition, the decomposition of $Ni(Ac)_2 \cdot 4H_2O/10\%$ $Cu(Ac)_2 \cdot H_2O$, and $Ni(Ac)_2 \cdot 4H_2O/10\%$ $Mn(Ac)_2$ also in TOP only at 300 °C for 1 hour yielded nickel phosphide, which matched well to NiP-1 (ICDD #03-065-1989) as shown in (Fig. S3b and c†). This result indicates that the surfactants (TOPO/HDA) also play a role in the phase transformations we observed in this study.

The morphology of formed and transformed nickel phosphides was studied by scanning electron microscopy (SEM).

SEM images show the formation of polydispersed hexagonal disc-shaped particles with some degree of truncated edges for Ni_2P formed from the decomposition of $Ni(Ac)_2 \cdot 4H_2O$ in TOPO/TOP i.e., NiP-1 (Fig. 4a). The discs which are placed perpendicular to the plane of the paper are observed as elongated or rod-like particles. The defined shape was converted to irregularly shaped particles aggregated together on doping with Cu (NiP-3) and Mn (NiP-4), which resulted in phase transformations (Fig. 4b, c and S4†). The morphology of the Ni_5P_4 formed from the decomposition of $Ni(Ac)_2 \cdot 4H_2O$ in HDA/TOP, i.e., NiP-2 as well as the Cu (NiP-5) and Mn (NiP-6) doped materials was shown by SEM images to be spherical, agglomerated, and well distributed (Fig. 4d–f and S5†).

Transmission electron microscopy (TEM) was employed to further probe the morphology of the formed and transformed phosphides. TEM images confirm the multi-shaped particles formed in NiP-1, NiP-3 and NiP-4 as well as the agglomeration in them as shown in the SEM analysis. It can be seen that the morphology of the initial parent phase and the transformed phase on doping (i.e., NiP-1, NiP-3 and NiP-4), is comparable (Fig. 5a–c). However, changing the surfactant significantly altered the size and morphology of the synthesized materials (Fig. 5d–f). It shows that the reactions performed in a given solvent system (TOPO/TOP or HDA/TOP) have almost similar morphology irrespective of the type of dopants. This kind of morphological conservation on transformation from one material to another has been documented.[33,46] Energy-dispersive X-ray spectroscopy (EDX) analysis confirms the
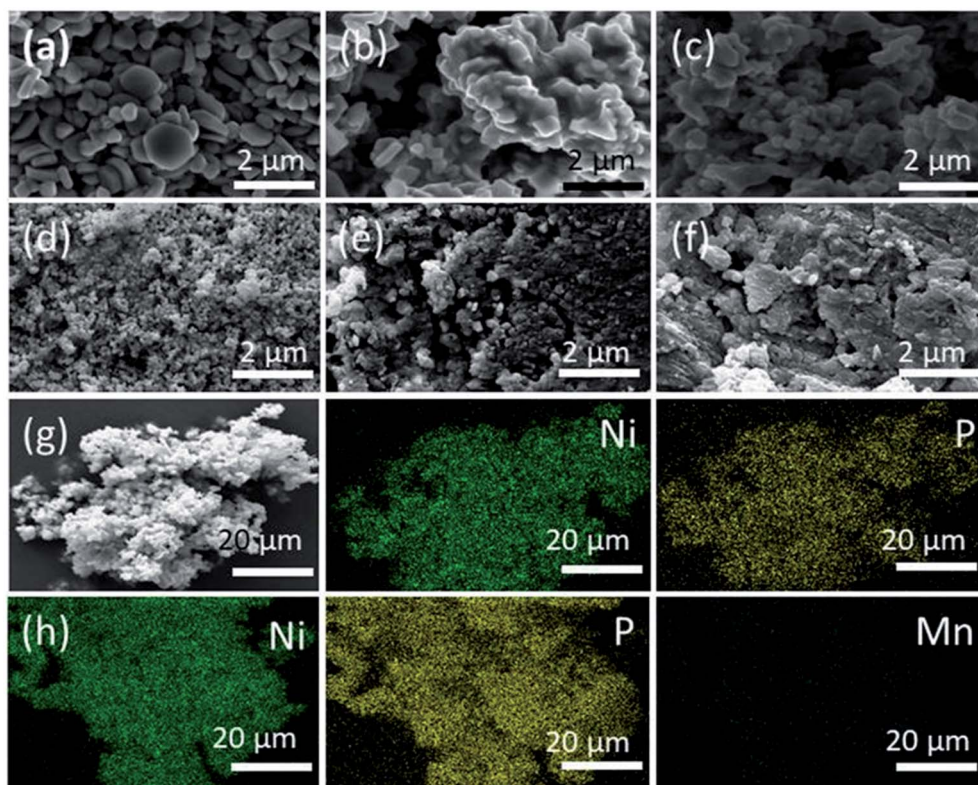

Fig. 4 SEM images of (a) NiP-1, (b) NiP-3 (c) NiP-4 (d) NiP-2 (e) NiP-5 and (f) NiP-6. Representative EDX elemental mapping images of (g) NiP-1 and (h) NiP-2.
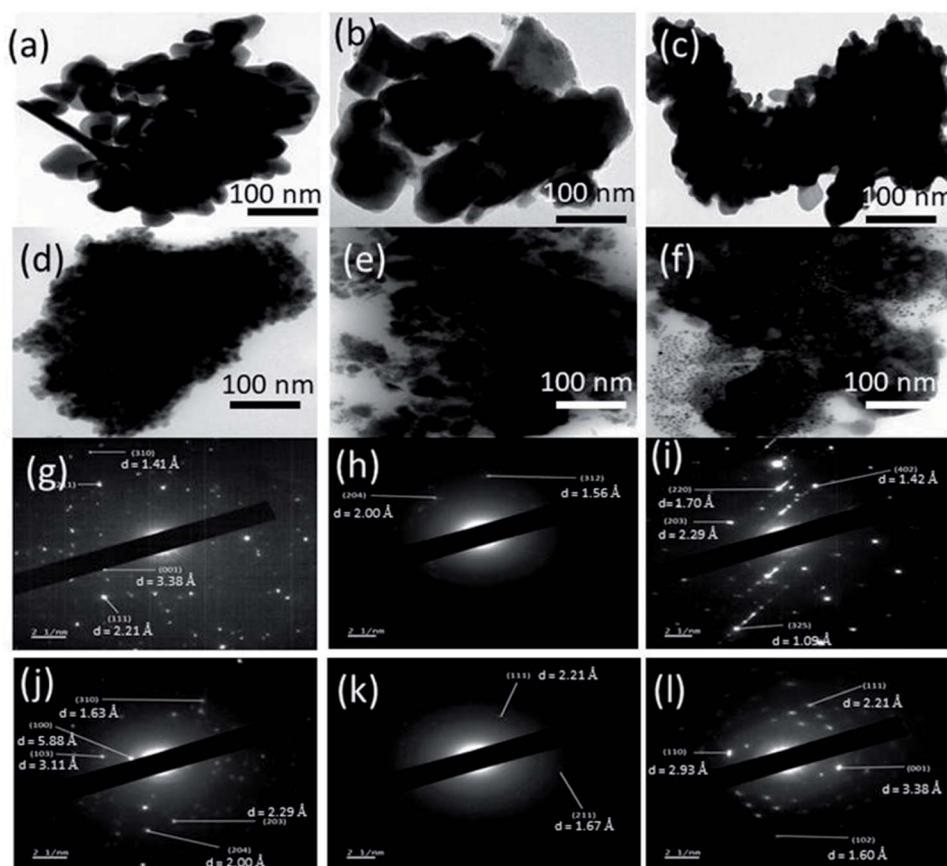
Fig. 5 TEM images of (a) NiP-1, (b) NiP-3 (c) NiP-4 (d) NiP-2 (e) NiP-5 and (f) NiP-6. SAED images of (g) NiP-1, (h) NiP-3 (i) NiP-4 (j) NiP-2 (k) NiP-5 and (l) NiP-6.

composition of the formed phosphides and incorporation of dopants (Cu or Mn) in transformed phosphides' lattices. The SEM-EDX elemental mapping of representative samples (Fig. 4g, h, S5 and S6†) indicate the uniform distribution of Ni, P and the dopants (Cu or Mn). Selected area electron diffraction (SAED) analysis of representative samples was performed to gain insight into the crystallinity of formed and transformed phosphides. Our materials showed well-defined SAED spots, which matched well with the lattice planes of hexagonal Ni_2P or Ni_5P_4 (Fig. 5g–i), indicating crystallinity.

Electrochemical properties of nickel phosphides for supercapacitor applications

The charge storage capability of formed nickel phosphides (NiP-1 and NiP-2) and the transformed ones (NiP-3 to NiP-6) were studied employing cyclic voltammetry (CV) and galvanostatic charge–discharge (GCD) measurements. The CV profile of all the nickel phosphide electrodes, which is a plot of the current density *versus* the electric potential of these electrodes, are given in Fig. 6. These CV profiles were recorded in the range of 0–0.6 (V, Hg/HgO) in 3 M KOH electrolyte and at scan rates ranging from 2 to 300 mV s^{-1}. All the nickel phosphide electrodes showed defined redox peaks for the oxidation and reduction processes indicative of typical pseudo-capacitance
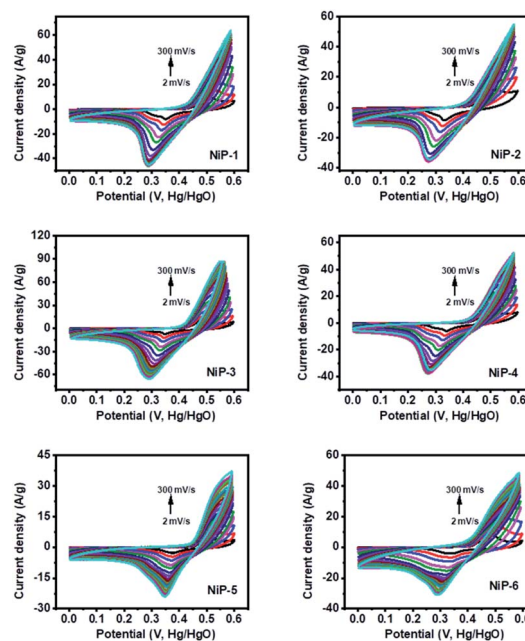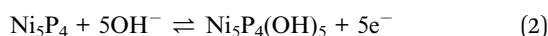

Fig. 6 CV curves of all the electrodes at different scan rates.

characteristics.[15,47] Also, the CV curves of all the electrodes were maintained even at high scan rates, as shown in Fig. 6, pointing to good redox reversibility.[2,48] The specific capacitance of all electrodes was calculated by integrating the plot area within the CV's curve following eqn (1).

$$C_{(\mathrm{F~g}^{-1})} = \frac{A}{m \times \Delta V \times \frac{\delta v}{\delta t}} \qquad (1)$$

where $C_{(\mathrm{F~g}^{-1})}$ is the specific capacitance in F g^{-1}, A is the area under the CV curve in cm^2, m is the mass of the electrode in g, $\frac{\delta v}{\delta t}$ is scan rate in V s^{-1}, and ΔV is the potential window in V. It is important to note that the CV curves of NiP-3 showed pairs of distinct redox peaks (anodic peak $\approx$ +0.55 V and cathodic peak $\approx$ +0.28 V) corresponding to Ni^{2+}/Ni^{3+} redox transitions similar to the study by Liu et al.[49] All the nickel phosphide electrodes also showed the Ni^{2+}/Ni^{3+} redox transitions (illustrated in eqn (2) and (3)) typical of faradaic capacitive behavior of the battery-type.

$$\mathrm{Ni_5P_4 + 5OH^- \rightleftharpoons Ni_5P_4(OH)_5 + 5e^-} \qquad (2)$$

$$\mathrm{Ni_2P + 2OH^- \rightleftharpoons Ni_2P(OH)_2 + 2e^-} \qquad (3)$$

GCD curves of all the nickel phosphide electrodes, which were obtained by analyzing the electrochemical performance of these electrodes in terms of potential (V, Hg/HgO) versus time (s) was employed to further probe the electrodes' capacitive behavior. The GCD profiles (Fig. 7) showed typical pseudo-capacitance behavior for all the electrodes which is in agreement with the CV results. NiP-2 showed the highest calculated
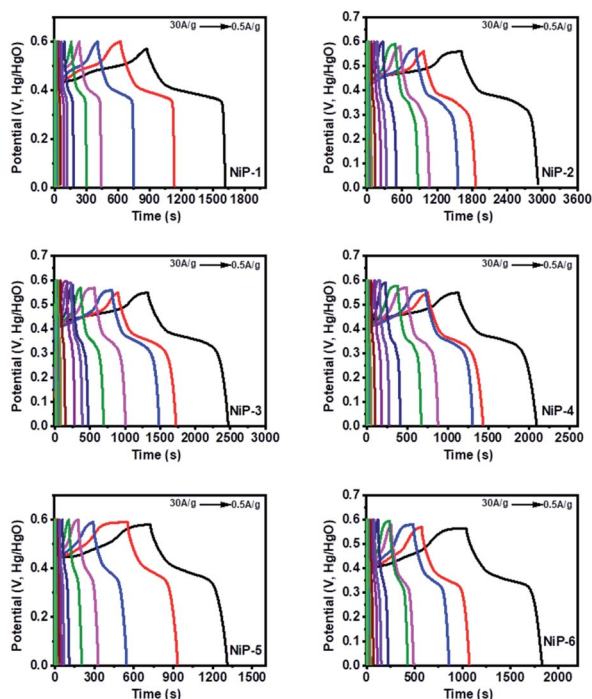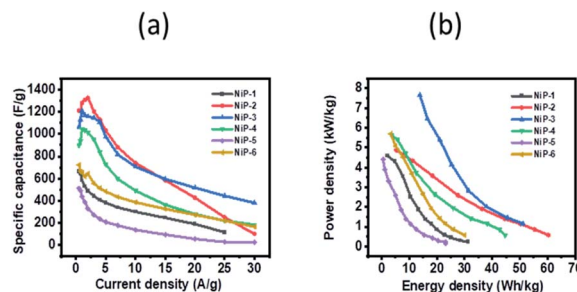

Fig. 8 (a) Variation of specific capacitance as a function of current density and (b) Ragone plots for the nickel phosphide samples.

specific capacitance of 1325 F g^{-1} at 2 A g^{-1}. The rate performance of NiP-2, however, dropped to 102 F g^{-1} as the charge and discharge current density increased to 30 A g^{-1}. It is pertinent to note that NiP-3 (Ni$_5$P$_4$ formed on doping Ni$_2$P with 10% Cu) with a calculated specific capacitance of 1209 F g^{-1} at 1 A g^{-1} had a better rate performance of 382 F g^{-1} at 30 A g^{-1}, which was the highest among the other samples at the same current density. It can be inferred from these results that Ni$_5$P$_4$ has better storage capacity compared to Ni$_2$P and that the presence of Cu in Ni$_5$P$_4$ dramatically improved its charge retention capacity even with an increase in the current density. The electrostatic interaction of Cu^{2+} with the P=O group of the branched surfactant TOPO plausibly maintained the redox process of NiP-3 at a high current density. The variation of specific capacitance and discharge current and the Ragone plot, a variation of energy density and power density for all the electrodes, are given in Fig. 8. Lu et al. prepared Ni$_2$P coated with Ni by an electroless process with a calculated specific capacitance of 464 F g^{-1}, which our NiP-2 electrode (1325 F g^{-1}) outperformed by 65%.[50] Similarly, the NiP-3 electrode (1209 F g^{-1}) showed better storage capacity compared to our earlier report of Ni$_2$P, Co–Ni$_2$P (864 F g^{-1}) and Fe–Ni$_2$P (856 F g^{-1}).[15]

Our nickel phosphide electrodes, therefore, showed better or competitive charge storage capacity in comparison to other similar reports (Table S1†).

The wide-scale application of supercapacitors is usually constrained by low energy density. We, therefore, calculated the energy density and power density of our electrodes using the following equations.

$$E = \frac{C_{\mathrm{sp}} \times (\Delta V)^2}{7.2} \qquad (4)$$

where E is energy density in W h kg^{-1}, C_{sp} is specific capacitance in F g^{-1}, and ΔV is the potential window for discharge.

$$P = \frac{E \times 3600}{t} \qquad (5)$$

where P is power density in kW kg^{-1}, E is energy in W h kg^{-1} and t is the discharge time in s.

The NiP-3 electrode gave the highest power density of 7.5 kW kg^{-1} and a calculated energy density of 51 W h kg^{-1}. The highest energy density of 60 W h kg^{-1} was, however, obtained from the NiP-2 electrode.
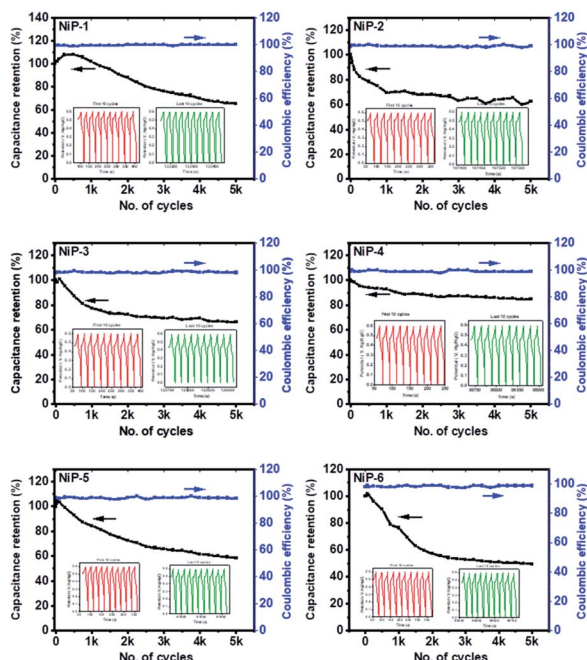

Fig. 7 GCD curves for all the electrodes at different scan rates.

Fig. 9 Electrochemical stability test up to 5000 cycles for the nickel phosphide samples.

Fig. 11 Polarization curves for HER at 1 and 1000 cycles for all the electrodes.

We also measured the long-term charge retention stability of our phosphide electrodes since this could limit their practical application and is presented in Fig. 9.

All the nickel phosphide electrodes showed an excellent charge retention capacity of $\approx 99\%$ even after 5000 cycles, suggestive of good cyclic stability. The CV and GCD measurements, therefore, indicate that formed nickel phosphides are electroactive materials employable in energy storage applications and that phase transformation on Cu doping in TOPO/TOP improves this process.

Water splitting applications of nickel phosphide electrodes

Hydrogen evolution reaction (HER). The evolution of hydrogen *via* water-splitting is one of the cleanest ways to generate energy and is therefore highly sought after today. However, the thermodynamic potential of ≈ 1.23 V is needed to generate hydrogen fuel from water splitting though this value is higher in reality.[3] The extra potential required to produce green
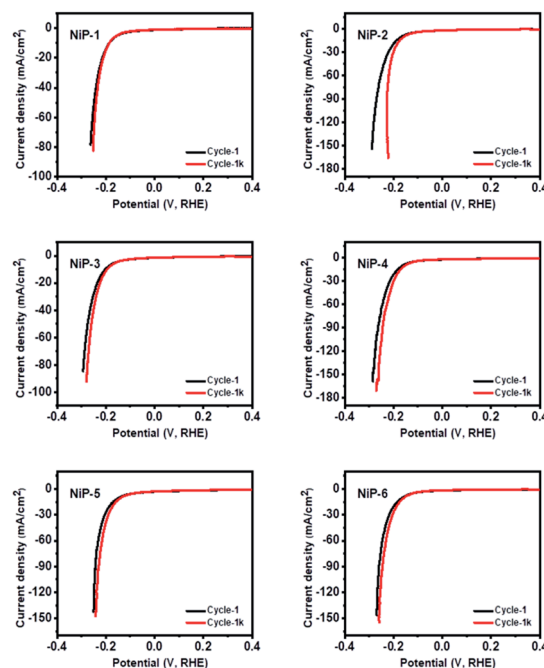

Fig. 10 HER performance of all the electrodes in terms of (a) overpotential and (b) Tafel slope.

hydrogen fuel is called overpotential. The formed nickel phosphide materials were therefore investigated for their electrocatalytic performance in reducing this constraining overpotential. Linear sweep voltammetry (LSV) measurements were employed to study the activity and stability of the electrodes (1 M KOH electrolyte) for HER and are given in Fig. 10 and 11. NiP-1 (Ni_2P) and NiP-2 (Ni_5P_4) formed from the decomposition of $Ni(Ac)_2 \cdot 4H_2O$ in TOPO/TOP and HDA/TOP required overpotentials of 186 and 167 mV to reach a current density of 10 mA cm^{-2}, respectively. NiP-1 and NiP-2 electrodes also had plotted Tafel slopes of 100 and 109 mV dec^{-1} indicative of fast reaction kinetics. The phosphorus richer NiP-1 performed better in reducing the overpotential in HER compared to NiP-1, just like in the charge storage supercapacitor applications, though with lower reaction kinetics. This agrees with documented reports[9,51] that have indicated that increasing the phosphorus content of metal phosphides improves their catalytic activity. The transformed nickel phosphides, Ni_2P (NiP-3, NiP-4) and Ni_5P_4 (NiP-5, NiP-6), however, required overpotentials of 203, 162, 146 and 164 mV to deliver a current density of 10 mA cm^{-2} along with Tafel slopes of 145, 109, 116 and 133 mV dec^{-1}, respectively. It is important to note that phase transformations resulting in Ni_5P_4 outperform the ones of Ni_2P in both reducing the overpotential and giving faster reaction kinetics. All the phase transformed electrodes (obtained on doping Cu and Mn) performed better in reducing the overpotential in HER compared to the pristine nickel phosphides except NiP-3. Doping the formed Ni_2P and Ni_5P_4 with Cu and Mn which resulted in phase transformations, therefore, improved their electrocatalytic activity in water splitting to generate hydrogen fuel. It is pertinent to note that the
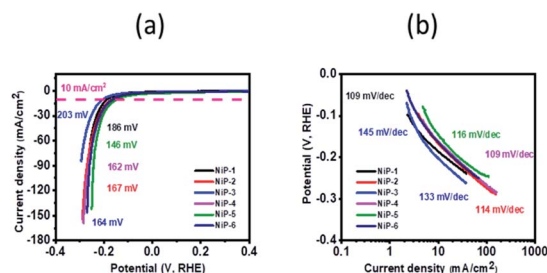
electrochemical activity of a catalyst can be a function of its d-band.[43] The d-band of a catalyst can be modulated by structural and chemical processes like variation of its particle size, substitution, intercalation and inducement of strain *via* doping. The improvement of our nickel phosphide catalysts' HER activity on doping/phase transformations could be due to their d-band alteration arising from the probable strain induced by transition metal doping. Researchers have employed this strategy in documented reports to boost the HER activity of their prepared catalyst.[43,52–54]

Kucernak and Sundaram[51] prepared nickel phosphides, Ni_2P and $Ni_{12}P_5$, by a mechano-chemical and hydrothermal route which required approximate overpotentials of 270 and 450 mV to reach a current density of 10 mA cm^{-2}, respectively which are outperformed by all our electrodes with our NiP-5 electrode (146 mV) outperforming them by 58 and 68%, respectively. Similarly, our nickel phosphide electrodes recorded lower overpotentials to deliver 10 mA cm^{-2} current density compared to nickel phosphide electrodes prepared by Yan *et al.* that required 310 mV to reach the same current density.[55] Pristine Ni_2P and doped-Ni_2P (Co–Ni_2P, Fe–Ni_2P) prepared by the hot injection route in our earlier study needed overpotentials of 164, 158 and 202 mV to deliver a current density of 10 mA cm^{-2} which is comparable to this study.[15] Similarly, bare dinickel phosphide recently prepared by a solvent-less route delivered a current density of 10 mA cm^{-2} with an overpotential of 174 mV comparable to our nickel phosphides.[3] Table S2† summarizes the HER performance of our electrodes in comparison to other nickel phosphides which indicates that our electrodes outperform or compare well with them.

The durability and long-term stability of an electrode are crucial factors necessary for the practical use of HER technologies.[56] We, therefore, investigated the long-term stability of our nickel phosphide electrodes by measuring their polarization curves which are given in Fig. 11. The polarization curves for all the electrodes in the 1st and 1000th cycles of recycling CV measurements show negligible deviation. A closer examination of the cycles for pristine Ni_5P_4 (NiP-2) and the doped-Ni_5P_4 (NiP-5 and NiP-6 obtained by phase transformation) indicate better electrode durability on phase transformation. These similar LSV-CV curves (Fig. 11) indicate that our electrodes maintained their electrochemical behavior for different cycles pointing to electrochemical stability and robusticity. We also analysed the powder XRD patterns of our catalysts prior to and after the HER tests to gain further insight into the stability of our nickel phosphide catalysts with the representative results given in Fig. S8.† These analyses clearly show that our catalysts are stable with similar XRD patterns prior to and after HER.

Oxygen evolution reaction (OER)s. The electrocatalytic performance of the formed and transformed phosphides towards OER was also investigated in 1 M KOH employing a three-electrode system. Fig. 12 shows LSV curves of all the nickel phosphide electrodes as well as the Tafel slopes. Traditionally the OER investigations of an electrode are done by measuring the overpotential required to reach a current density of 10 mA cm^{-2}. NiP-1, NiP-2, NiP-3, NiP-4, NiP-5, and NiP-6 required overpotentials of 344, 324, 276, 324, 347, 345 mV to
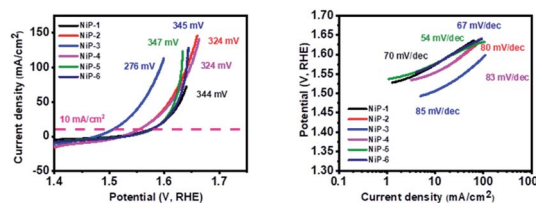

Fig. 12 LSV plots and Tafel slopes for nickel phosphide electrodes for OER.

deliver a current density of 10 mA cm^{-2} alongside Tafel slopes of 70, 80, 85, 83, 54, and 67 mV dec^{-1}, respectively. The phase transformed electrodes generally decreased the constraining overpotentials of the pristine nickel phosphides for OER except for NiP-5. NiP-3 required the least overpotential (276 mV) among all the samples to reach a current density of 10 mA cm^{-2}.

NiP-5 had the lowest Tafel slope of 54 mV dec^{-1} among all the samples, indicative of the fastest reaction kinetics. Therefore NiP-3 was a better catalyst in overcoming the thermodynamic barrier for OER while NiP-5 catalyst had the fastest reaction kinetics. Furthermore, phase transformation upon Cu and Mn doping, therefore, improved the nickel phosphides' reaction kinetics. The lower overpotential of NiP-3 (Ni_5P_4, 10% Cu) may be attributed to the presence of Cu in the Ni_5P_4 lattice, which probably leads to more exposed active sites for the adsorption of OH$^-$ species for the formation of O_2.[57] This may be due to the fact that doping a foreign atom into a host material lattice generally alters its electronic and atomic environment.[58] Furthermore, documented reports[59,60] indicate that the stretching or compression of atoms in the lattice of a catalyst induced by doping that leads to strain improves a catalyst's OER activity. The probable strain in the transformed nickel phosphides on doping Cu and Mn improves the catalyst's OER activity. It is important to note that NiP-3 with the slowest reaction kinetics (85 mV dec^{-1}) among all the samples has a faster reaction kinetics than the state-of-art IrO_2 for OER which is ≈124.5 mV dec^{-1}. Additionally, our nickel phosphide electrodes compare well or outperform other reported nickel phosphides (Table S3†).

The practical application of an electrode for OER is a function of its long-term stability and durability. The LSV-CV curves of all the electrodes for the 1st and 1000th cycles were therefore measured and are given in Fig. 13. These LSV curves matched well, indicating good stability. Also, the stability of all materials as OER catalysts was studied using chronoamperometry (CA) measurements at a constant voltage of 0.55 V for 25 h. As shown in Fig. 14, all electrodes maintained a high current for an extended time. NiP-3 displayed the highest current density value of 27.5 mA cm^{-2} and a stable current through the experiment, indicating excellent electrochemical stability. Moreover, Fig. 14 also indicates that phase transformation in the nickel phosphide system improved the catalyst's durability and stability. Powder XRD pattern examinations of our nickel phosphides prior to and after OER also indicated catalysts stability as well as robusticity which is given by a representative example in Fig. S9.†
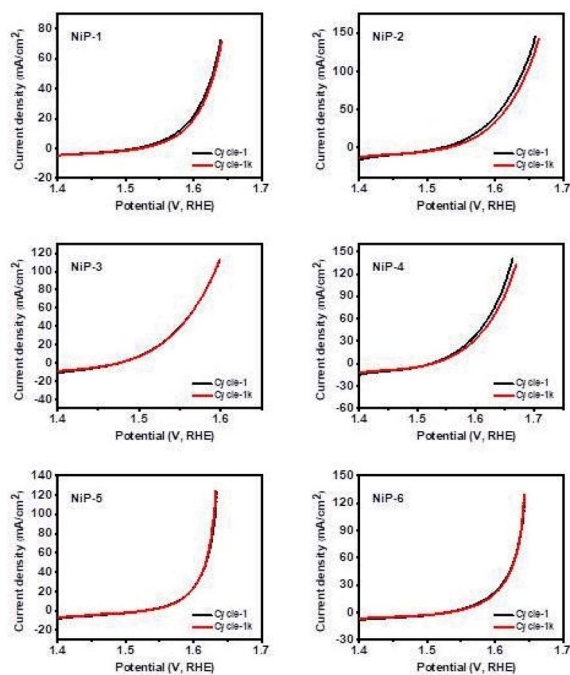
Fig. 13 LSV-CV stability curves in 1000 cycles of all nickel phosphide electrodes for OER.

This experiment, therefore, demonstrated that our nickel phosphide electrodes could maintain their performance for an extended period. It is important to note that the slight fluctuations observed in some of the plots are related to the bubbling of O_2 that is released during the OER process.[3]
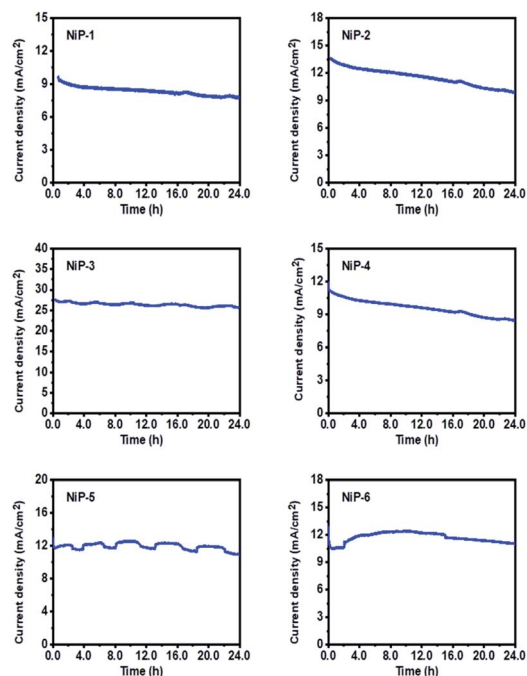
The electrochemical impedance spectroscopy (EIS) measurements for all the electrodes were also performed to gain further insight into the effect of phase transformations in the nickel phosphide system upon doping with transition metals. These EIS measurements in the form of Nyquist plots (Fig. 15) were therefore obtained by applying a frequency range from 0.05 Hz to 10 kHz along with the applied alternate current amplitude of 10 mV. Also, the electric potentials of 0.45, 0.5, 0.55, and 0.6 V for each sample were employed using a saturated calomel electrode (SCE) as reference. The diameter of the semicircle or arc is directly related to the resistance of the charge transfer process, meaning that a smaller diameter gives a lower charge transfer resistance.[58] The resistance measurements of all the electrodes in decreasing order is NiP-1 > NiP-5 > NiP-3 > NiP-4 > NiP-2 > NiP-6. Hence doping NiP-1 with Cu (NiP-3) and Mn (NiP-4), decreased the charge transfer resistance, as shown in Fig. 15. NiP-6 showed the best electron transfer process among the other electrodes. Similarly, doping NiP-2 (Ni_5P_4 formed by the decomposition of $Ni(Ac)_2 \cdot 4H_2O$ in HDA/TOP) with Mn (NiP-6), which transformed Ni_5P_4 to Ni_2P decreased the EIS measurements comparatively. Only NiP-5 (Ni_5P_4 formed on Cu doping of Ni_2P) electrode among all the electrodes did not decrease the EIS measurements compared to the pristine phosphides. Moreover, it is important to note that NiP-5 and NiP-6 Nyquist plots showed two arcs, as seen in Fig. 15, which was also observable in our previous study.[15] When this behavior occurs, it means that the arc at high frequency represents the charge transfer resistance, which was observed in all the electrodes, whereas the arc at lower frequencies is related to mass transfer resistance.[61] Therefore, NiP-6 electrode among all samples offered the lowest charge transfer resistance and phase transformations in the nickel phosphide system

Fig. 14 Chronoamperometry measurements for all the electrodes at a constant voltage of 0.55 V.
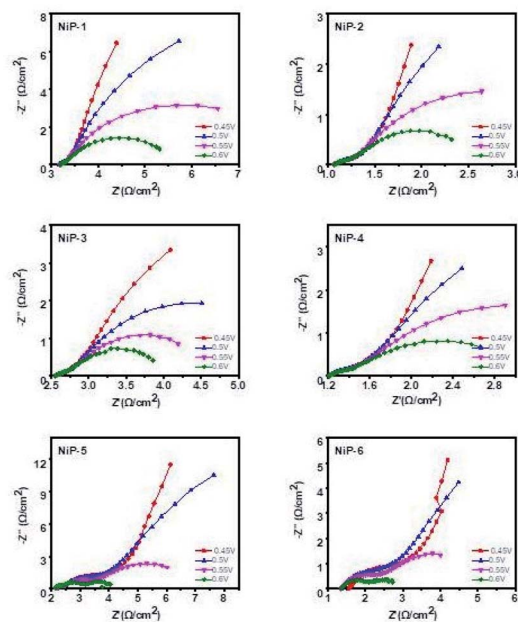

Fig. 15 EIS for all the electrodes represented as Nyquist plots at 0.45, 0.5, 0.55 and 0.6 V.

induced by transition metal doping decreased this charge transfer resistivity.

Considering all the OER performance indicators, we can therefore conclude that phase transformations in the nickel phosphide system upon doping with transition metals (Cu & Mn) resulted in better OER activity, performance, and stability, with the NiP-3 electrode having the best performance.

Conclusion

Different phases of nickel phosphides (Ni_2P and Ni_5P_4) can be prepared by the decomposition of $Ni(AC)_2 \cdot 4H_2O$ by a colloidal route (TOPO/TOP or HDA). The employed solvents and incorporation of transition metal (Cu or Mn) as dopants, results in either phase transformations (Ni_2P to Ni_5P_4 or Ni_5P_4 to Ni_2P) or formation of mixture of phases (Ni_2P/Ni_5P_4). The probable reasons for these rare transformations are discussed. The performance of pristine and transformed nickel phosphides as electrocatalysts was investigated for overall water splitting reactions, where the phase transformation resulted in an improved electrode's catalytic activity and durability. Upon doping with Cu, the transformed nickel phosphide phases showed the lowest overpotentials for both HER and OER (*i.e.*, current density of 10 mA cm^{-2} was achieved at an overpotential of 146 mV for HER and overpotential of 276 mV for the OER at the same current density). NiP-2 had the highest calculated specific capacitance of 1325 at 2 A g^{-1}. All electrodes showed good stability and durability, which are crucial to practical application in green hydrogen generation technologies.

Author contributions

Gwaza E. Ayom: conceptualization, investigation, methodology, writing-original draft, writing-review and editing. Malik D. Khan: conceptualization, validation, writing-review and editing. Siphamandla C. Masikane: data acquisition for SEM & TEM. Felipe M. de Souza: writing-the electrochemical part. Wang Lin: data acquisition for the electrochemical part. Ram Gupta: writing-review of the electrochemical part and supervision of electrochemical data acquisition. Neerish Revaprasadu: supervision, funding acquisition, resources and writing-editing.

Conflicts of interest

There are no conflicts to declare.

Acknowledgements

References

1 W. Li, M. Wu, P. Shi, T. Li, H. Yue, Z. Dong, Y. Gao and X. Lou, *Electrochim. Acta*, 2020, **331**, 135440.

2 G. E. Ayom, M. D. Khan, T. Ingsel, W. Lin, R. K. Gupta, S. J. Zamisa, W. E. van Zyl and N. Revaprasadu, *Chem.–Eur. J.*, 2020, **26**, 2693–2704.

3 G. E. Ayom, M. D. Khan, G. B. Shombe, J. Choi, R. K. Gupta, W. E. van Zyl and N. Revaprasadu, *Inorg. Chem.*, 2021, **60**, 11374–11384.

4 M. Dilshad Khan, S. U. Awan, C. Zequine, C. Zhang, R. K. Gupta and N. Revaprasadu, *ACS Appl. Energy Mater.*, 2020, **3(2)**, 1448–1460.

5 P. Kannan, T. Maiyalagan, B. Lin, W. Lei, C. Jie, L. Guo, Z. Jiang, S. Mao and P. Subramanian, *Talanta*, 2020, **209**, 120511.

6 U. Guharoy, T. Ramirez Reina, E. Olsson, S. Gu and Q. Cai, *ACS Catal.*, 2019, **9**, 3487–3497.

7 S. Zhang, G. Gao, H. Zhu, L. Cai, X. Jiang, S. Lu, F. Duan, W. Dong, Y. Chai and M. Du, *Sci. Bull.*, 2020, **65**, 640–650.

8 Z. Zhu, J. Hao, H. Zhu, S. Sun, F. Duan, S. Lu and M. Du, *Adv. Fiber Mater.*, 2021, **3**, 117–127.

9 A. Ray, S. Sultana, L. Paramanik and K. M. Parida, *J. Mater. Chem. A*, 2020, **8**, 19196–19245.

10 C. Hu, C. Lv, S. Liu, Y. Shi, J. Song, Z. Zhang, J. Cai and A. Watanabe, *Catalysts*, 2020, **10**, 188.

11 Y. Gan, C. Wang, X. Chen, P. Liang, H. Wan, X. Liu, Q. Tan, H. Wu, H. Rao and H. Wang, *Chem. Eng. J.*, 2020, **392**, 123661.

12 H. Kim, S. Surendran, Y. Chae, H. Y. Lee, T.-Y. An, H. S. Han, W. Park, J. K. Kim and U. Sim, *Appl. Surf. Sci.*, 2020, **511**, 145424.

13 J. Liu, X. Chen, M. Shao, C. An, W. Yu and Y. Qian, *J. Cryst. Growth*, 2003, **252**, 297–301.

14 S. Yang, G. Chen, A. G. Ricciardulli, P. Zhang, Z. Zhang, H. Shi, J. Ma, J. Zhang, P. W. Blom and X. Feng, *Angew. Chem., Int. Ed.*, 2020, **59**, 465–470.

15 G. E. Ayom, M. D. Khan, J. Choi, R. K. Gupta, W. E. van Zyl and N. Revaprasadu, *Dalton Trans.*, 2021, **50(34)**, 11821–11833.

16 W. Han, X. Li, B. Liu, L. Li, H. Tang, Y. Li, C. Lu and X. Li, *Chem. Commun.*, 2019, **55**, 9279–9282.

17 G. E. Ayom, M. D. Khan, G. B. Shombe, J. Choi, R. K. Gupta, W. E. van Zyl and N. Revaprasadu, *Inorg. Chem.*, 2021, **60(15)**, 11374–11384.

18 J. F. Callejas, C. G. Read, C. W. Roske, N. S. Lewis and R. E. Schaak, *Chem. Mater.*, 2016, **28**, 6017–6044.

19 C. Guo, X. Liu, L. Gao, X. Kuang, X. Ren, X. Ma, M. Zhao, H. Yang, X. Sun and Q. Wei, *Appl. Catal., B*, 2020, **263**, 118296.

20 J. Xu, Z. Liu, Z. Wei, S. Zhang, C. Guo and M. He, *Electrochim. Acta*, 2020, 136417.

21 C. Wei, X. Fan, X. Deng, L. Ma, X. Zhang, Q. Liu and J. Guo, *Sustainable Energy Fuels*, 2020, **4**, 1883–1890.

22 S. Xu, Y. Du, X. Liu, X. Yu, C. Teng, X. Cheng, Y. Chen and Q. Wu, *J. Alloys Compd.*, 2020, 154210.

23 Y. Zhang, L. Sun, L. Bai, H. Si, Y. Zhang and Y. Zhang, *Nano Res.*, 2019, **12**, 607–618.

24 W. S. Leong, *Nature*, 2020, **577**, 477–478.

25 H. Asayesh-Ardakani, A. Nie, P. M. Marley, Y. Zhu, P. J. Phillips, S. Singh, F. Mashayek, G. Sambandamurthy, K.-b. Low and R. F. Klie, *Nano Lett.*, 2015, **15**, 7179–7188.

26 Y.-R. Zheng, P. Wu, M.-R. Gao, X.-L. Zhang, F.-Y. Gao, H.-X. Ju, R. Wu, Q. Gao, R. You and W.-X. Huang, *Nat. Commun.*, 2018, **9**, 1–9.

27 D. Voiry, H. Yamaguchi, J. Li, R. Silva, D. C. Alves, T. Fujita, M. Chen, T. Asefa, V. B. Shenoy and G. Eda, *Nat. Mater.*, 2013, **12**, 850–855.

28 M. A. Lukowski, A. S. Daniel, F. Meng, A. Forticaux, L. Li and S. Jin, *J. Am. Chem. Soc.*, 2013, **135**, 10274–10277.

29 H. Huang, X. Fan, D. J. Singh and W. T. Zheng, *Nanoscale*, 2020, **12**(3), 1247–1268.

30 D. Pariari, R. M. Varma, M. N. Nair, P. Zeller, M. Amati, L. Gregoratti, K. K. Nanda and D. Sarma, *Appl. Mater. Today*, 2020, **19**, 100544.

31 S. Demirci, H. H. Gürel, J. Seymur and S. Ciraci, *Nanoscale*, 2020, **12**(5), 3249–3258.

32 G. B. Shombe, M. D. Khan, C. Zequine, C. Zhao, R. K. Gupta and N. Revaprasadu, *Sci. Rep.*, 2020, **10**, 1–14.

33 E. Muthuswamy and S. L. Brock, *Chem. Commun.*, 2011, **47**, 12334–12336.

34 S. Lu, H. Xu, B. Gao and L. Ren, *New J. Chem.*, 2017, **41**, 8497–8502.

35 H. Xu, S. Lu and L. Ren, *Mater. Res. Express*, 2016, **3**, 105010.

36 K. Aso, A. Hayashi and M. Tatsumisago, *Inorg. Chem.*, 2011, **50**, 10820–10824.

37 W. Wang, B. Gu and L. Liang, *J. Dispersion Sci. Technol.*, 2005, **25**, 593–601.

38 I. Csik, S. P. Russo and P. Mulvaney, *J. Phys. Chem. C*, 2008, **112**, 20413–20417.

39 W. W. Yu, Y. A. Wang and X. Peng, *Chem. Mater.*, 2003, **15**, 4300–4308.

40 D. Li, K. Senevirathne, L. Aquilina and S. L. Brock, *Inorg. Chem.*, 2015, **54**, 7968–7975.

41 P. Chen, K. Xu, S. Tao, T. Zhou, Y. Tong, H. Ding, L. Zhang, W. Chu, C. Wu and Y. Xie, *Adv. Mater.*, 2016, **28**, 7527–7532.

42 S. Sarkar, L. Dheer, C. Vinod, R. Thapa, U. V. Waghmare and S. C. Peter, *ACS Appl. Energy Mater.*, 2020, **3**, 1271–1278.

43 S. C. Sarma, V. Mishra, K. A. Ann Mary, S. Roy and S. C. Peter, *ACS Energy Lett.*, 2018, **3**, 3008–3014.

44 E. Muthuswamy, G. H. L. Savithra and S. L. Brock, *ACS Nano*, 2011, **5**, 2402–2411.

45 L. Yu, J. Zhang, Y. Dang, J. He, Z. Tobin, P. Kerns, Y. Dou, Y. Jiang, Y. He and S. L. Suib, *ACS Catal.*, 2019, **9**, 6919–6928.

46 A. E. Henkes and R. E. Schaak, *Inorg. Chem.*, 2008, **47**, 671–677.

47 D. Guragain, C. Zequine, R. Bhattarai, J. Choi, R. K. Gupta, X. Shen and S. R. Mishra, *MRS Adv.*, 2020, **5**, 2487–2494.

48 I. Rabani, J. Yoo, C. Bathula, S. Hussain and Y.-S. Seo, *J. Mater. Chem. A*, 2021, **9**, 11580–11594.

49 S. Liu, K. V. Sankar, A. Kundu, M. Ma, J.-Y. Kwon and S. C. Jun, *ACS Appl. Mater. Interfaces*, 2017, **9**, 21829–21838.

50 Y. Lu, J.-k. Liu, X.-y. Liu, S. Huang, T.-q. Wang, X.-l. Wang, C.-d. Gu, J.-p. Tu and S. X. Mao, *CrystEngComm*, 2013, **15**, 7071–7079.

51 A. R. Kucernak and V. N. N. Sundaram, *J. Mater. Chem. A*, 2014, **2**, 17435–17445.

52 K. Yan, S. K. Kim, A. Khorshidi, P. R. Guduru and A. A. Peterson, *J. Phys. Chem. C*, 2017, **121**, 6177–6183.

53 H. Zhu, G. Gao, M. Du, J. Zhou, K. Wang, W. Wu, X. Chen, Y. Li, P. Ma and W. Dong, *Adv. Mater.*, 2018, **30**, 1707301.

54 I. Roger, R. Moca, H. N. Miras, K. G. Crawford, D. A. Moran, A. Y. Ganin and M. D. Symes, *J. Mater. Chem. A*, 2017, **5**, 1472–1480.

55 L. Yan, P. Dai, Y. Wang, X. Gu, L. Li, L. Cao and X. Zhao, *ACS Appl. Mater. Interfaces*, 2017, **9**, 11642–11650.

56 Y. Wen, Z. Zhuang, H. Zhu, J. Hao, K. Chu, F. Lai, W. Zong, C. Wang, P. Ma and W. Dong, *Adv. Energy Mater.*, 2021, **11**, 2102138.

57 B. Qiu, L. Cai, Y. Wang, Z. Lin, Y. Zuo, M. Wang and Y. Chai, *Adv. Funct. Mater.*, 2018, **28**, 1706008.

58 J. Kundu, S. Khilari, K. Bhunia and D. Pradhan, *Catal. Sci. Technol.*, 2019, **9**, 406–417.

59 N. Ma, N. Li, T. Wang, X. Ma and J. Fan, *J. Mater. Chem. A*, 2021, **10**(3), 1390–1401.

60 X. Gao, Y. Zhou, Y. Tan, S. Liu, Z. Cheng and Z. Shen, *Phys. Chem. Chem. Phys.*, 2020, **22**, 2457–2465.

61 Q.-A. Huang, R. Hui, B. Wang and J. Zhang, *Electrochim. Acta*, 2007, **52**, 8144–8164.